


Three-dimensional numerical study on wrinkling of vesicles in elongation flow based on the immersed boundary method


Wang Xiao ¹, Kai Liu,^{2,*} John Lowengrub,³ Shuwang Li,⁴ and Meng Zhao^{1,†}

¹*School of Mathematics and Statistics, Center for Mathematical Sciences, Huazhong University of Science and Technology, Wuhan 430074, China*

²*College of Education for the Future, Beijing Normal University, Zhuhai 519087, China*

³*Department of Mathematics, University of California Irvine, Irvine, California 92697, USA*

⁴*Department of Applied Mathematics, Illinois Institute of Technology, Chicago, Illinois 60616, USA*

 (Received 20 April 2022; revised 10 November 2022; accepted 15 February 2023; published 3 March 2023)

We study the wrinkling dynamics of three-dimensional vesicles in a time-dependent elongation flow by utilizing an immersed boundary method. For a quasispherical vesicle, our numerical results well match the predictions of perturbation analysis, where similar exponential relationships between wrinkles' characteristic wavelength and the flow strength are observed. Using the same parameters as in the experiments by Kantsler *et al.* [V. Kantsler *et al.*, *Phys. Rev. Lett.* **99**, 178102 (2007)], our simulations of an elongated vesicle are in good agreement with their results. In addition, we get rich three-dimensional morphological details, which are favorable to comprehend the two-dimensional snapshots. This morphological information helps identify wrinkle patterns. We analyze the morphological evolution of wrinkles using spherical harmonics. We find discrepancies in elongated vesicle dynamics between simulations and perturbation analysis, highlighting the importance of the nonlinear effects. Finally, we investigate the unevenly distributed local surface tension, which largely determines the position of wrinkles excited on the vesicle membrane.

DOI: [10.1103/PhysRevE.107.035103](https://doi.org/10.1103/PhysRevE.107.035103)

I. INTRODUCTION

Vesicles are sacs with fluid inside and have a nearly inextensible lipid-bilayer boundary. They are used to study fundamental physics for more complicated biological systems such as cells and microcapsules [1–3]. Vesicles also play a significant role in intracellular and extracellular transport processes, for example, the courier for drug delivery.

Equilibrium mechanical properties of vesicles are well understood. The nonequilibrium dynamics of the vesicle subjected to an external flow have received intensive attention in numerous theoretical [4–9], numerical [10–17], and experimental [18–25] studies, as comprehensively reviewed in [26].

When immersed in a viscous fluid, vesicles show rich phenomena and shape transitions induced by membrane elasticity, hydrodynamic flows, and thermal fluctuations [26,27]. The existing theoretical models and numerical approaches satisfactorily describe the properties of the tank-treading and tumbling motions in linear flows with both rotational and elongational components [15,20,21]. As the transition between these two regimes, strong shape deformations and amplification of thermal fluctuations generate a new regime called trembling [16,23]. Wrinkles were observed by Kantsler *et al.* for the first time [28]. Immediately after, Turitsyn *et al.* [29] studied the interaction between the vesicle shape and the wrinkle structure by perturbation analysis. From then

on, the transient dynamics of vesicle wrinkling has been the focus [10,11,30,31].

The vesicle wrinkling has been studied numerically in two dimensions (2D) before [10,11,32]. However, 2D results only provide limited information about wrinkles on the vesicle. Thus, a three-dimensional (3D) scheme is needed to investigate the dynamics. In [16], Yazdani and Bagchi investigated the 3D vesicle dynamics in a shear flow with 160^3 grids and 5120 triangles. However, we are concerned with small wrinkles on the vesicle, which require much finer meshes. As a consequence, a highly efficient parallel algorithm has to be implemented involving both fluid and vesicles.

To simulate the transient dynamics of a vesicle in a time-dependent elongation flow, we first establish a physical dynamical model which uses the Stokes equation to describe a viscous incompressible fluid and uses a simplified version of the Helfrich model to describe the vesicle [33]. Then, we implement the immersed boundary method efficiently using graphics processing unit (GPU) parallelization. The numerical results of the quasispherical vesicle are in outstanding agreement with the predictions of perturbation analysis. Similar exponential relationships between the characteristic wavelength of wrinkles and flow strength are found. For an elongated vesicle, our simulations match well with the experimental results under different flow strengths. We get bounteous 3D morphological details of the wrinkling behaviors, which helps comprehend 2D snapshots from the experiments. Under the experimental conditions that we set up, the transient wrinkles on the vesicle follow the highly disordered zigzag herringbone pattern [34,35]. In a strong

*liuk@bnu.edu.cn

†mzhao9@hust.edu.cn

flow, wrinkles tend to be peanut shaped. Finally, we use spherical harmonics to investigate the morphological evolution of wrinkles. Our findings are similar to those of the experiments. Wrinkles are concentrated on two symmetrical poles where the membrane is mostly compressed. We compare the vesicle shape with local surface tension under different flow strengths. A stronger flow speeds up the deformation and activates higher-order modes.

The paper is organized as follows. In Sec. II, we give the physical model of the vesicle wrinkling in an extensional flow. In Sec. III, we revisit a perturbation analysis of the quasispherical vesicle. In Sec. IV, we discuss the numerical methods. In Sec. V, we give numerical results and analysis. In Sec. VI, we give concluding remarks and discuss potential future work.

II. PHYSICAL MODEL

We study the evolution of a 3D vesicle in a viscous flow where the inner and outer fluid properties are matched. The surface area A_0 and volume V_0 of the vesicle are conserved. The extensional flow field \mathbf{u}^∞ is suddenly reversed at t_0 , which causes the vesicle to deform.

A. Vesicle

The bending energy \mathbf{E}_b is described by a Helfrich functional [4],

$$\mathbf{E}_b = \frac{\kappa}{2} \int_{\mathcal{S}} H^2 dA, \quad (1)$$

where κ is the bending stiffness, dA is the area element on the membrane \mathcal{S} , and H is the mean curvature.

The area of conservation is enforced by \mathbf{E}_σ ,

$$\mathbf{E}_\sigma = \int_{\mathcal{S}} \sigma dA. \quad (2)$$

In perturbation analysis, the surface tension σ is a Lagrange multiplier to enforce global area conservation [4,10,36,37]. Numerically, it is applied as a springlike energy, which simplifies the simulation. See Appendix A and Ref. [33] for details.

The total elastic energy reads

$$\mathbf{E} = \mathbf{E}_b + \mathbf{E}_\sigma = \int_{\mathcal{S}} \left(\frac{\kappa}{2} H^2 + \sigma \right) dA. \quad (3)$$

The elastic force is derived by an Euler-Lagrange equation,

$$\mathbf{F} = - \frac{\partial \mathbf{E}}{\partial \mathbf{X}}, \quad (4)$$

where \mathbf{X} is the position of the membrane. Following [33], this energy (3) is discretized by a triangular mesh, where the mean curvature H on a vertex is computed by the triangles connected to it. The discretized force is then derived by a variational approach via Eq. (4). See Appendix A for details.

B. Stokes flow

We consider a 3D vesicle immersed in a viscous fluid and containing the same fluid inside. The fluids inside and outside the vesicle are assumed to be highly viscous and satisfy the Stokes equation [10],

$$\mu \Delta \mathbf{u}_i(\mathbf{x}, t) - \nabla p_i = 0, \quad (5)$$

$$\nabla \cdot \mathbf{u}_i(\mathbf{x}, t) = 0, \quad (6)$$

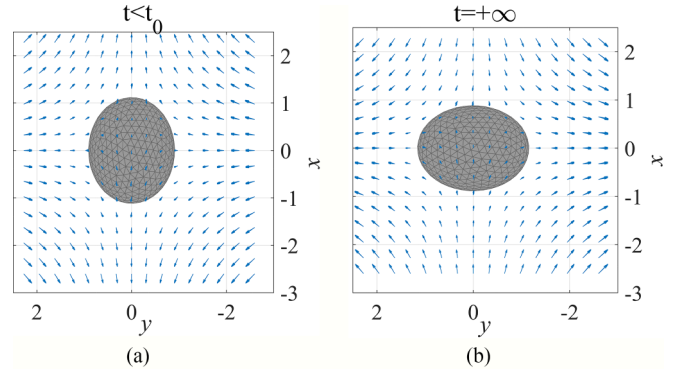


FIG. 1. Schematic diagrams of the vesicle and the velocity field around it. When the elongation flow is suddenly switched from (a) $u_x^\infty = \dot{\gamma}x$ and $u_y^\infty = -\dot{\gamma}y$ to (b) $u_x^\infty = -\dot{\gamma}x$ and $u_y^\infty = \dot{\gamma}y$ at t_0 , while u_z^∞ remains zero, the vesicle undergoes a relaxation from (a) one stretched stationary state to (b) another one. Here the values on the axes are nondimensionalized.

where $\mathbf{u}_i(\mathbf{x}, t)$ is the Eulerian velocity field of the fluid at the position $\mathbf{x} \in \mathbb{R}^3$ and time $t \in \mathbb{R}^+$ in the fluid domain Ω_i , $i = 1, 2$ refers to the fluid in and out of the vesicle, p_i is the pressure, and μ is the dynamic viscosity.

The velocity is continuous across the vesicle membrane \mathcal{S} . The hydrodynamic force and the elastic force at the membrane are balanced. So we have the following boundary conditions on \mathcal{S} :

$$\mathbf{u}_1|_{\mathcal{S}} - \mathbf{u}_2|_{\mathcal{S}} = 0, \quad (7)$$

$$[\mathbf{F}(\mathbf{x}, t) + (\mathbf{T}_1 - \mathbf{T}_2) \cdot \mathbf{n}]|_{\mathcal{S}} = 0. \quad (8)$$

Here, \mathbf{T}_i is the fluid stress tensor, \mathbf{n} is the unit normal vector of \mathcal{S} , and \mathbf{F} is the elastic force of the vesicle membrane.

We apply an external extensional flow field $\mathbf{u}^\infty(\mathbf{x}, t)$ for $\mathbf{x} \in \Omega$, where $\Omega = \Omega_1 \cup \Omega_2$. The external extensional flow $u_x^\infty = \dot{\gamma}x$, $u_y^\infty = -\dot{\gamma}y$, $u_z^\infty = 0$, where $\dot{\gamma}$ is the extensional rate. The total velocity field $\mathbf{u}(\mathbf{x}, t)$ is decomposed into the external elongational flow \mathbf{u}^∞ and the induced flow \mathbf{u}^{ind} due to the presence of the vesicle [10],

$$\mathbf{u}(\mathbf{x}, t) = \mathbf{u}^\infty(\mathbf{x}) + \mathbf{u}^{\text{ind}}(\mathbf{x}, t). \quad (9)$$

The vesicle moves with the fluid with velocity $\mathbf{u}(\mathbf{x}, t)$, as shown in Fig. 1. When the elongation flow is suddenly switched from $u_x^\infty = \dot{\gamma}x$ and $u_y^\infty = -\dot{\gamma}y$ to $u_x^\infty = -\dot{\gamma}x$ and $u_y^\infty = \dot{\gamma}y$ at t_0 , while u_z^∞ remains zero, the vesicle undergoes a relaxation from one stretched stationary state, as shown in Fig. 1(a), to another one, as shown in Fig. 1(b).

III. REVIEW OF PERTURBATION ANALYSIS

The excess area $\Delta = A/R^2 - 4\pi$ measures how spherical a vesicle is, with small Δ representing its proximity to a sphere. Here, R is the effective vesicle radius, defined as the radius of a sphere with the same volume as the vesicle.

The shape of a quasispherical vesicle ($\sqrt{\Delta} \ll 1$) reads

$$r(\theta, \phi) = R \left[1 + \sum_{l \geq 0} \sum_{m=-l}^l \sqrt{\frac{\Delta}{(l-1)(l+2)}} u_{l,m}(t) Y_{l,m}(\theta, \phi) \right], \quad (10)$$

where $Y_{l,m}(\theta, \phi)$ is the spherical harmonics of mode (l, m) at (θ, ϕ) [4]. Here, $u_{l,m}(t)$ is the scaled amplitude for each mode. The gradient component of the external field velocity is $\dot{\gamma} = 11\sqrt{5}/(16\sqrt{6\pi})S(t)\sqrt{\Delta}/\tau$, and $\tau = \mu R^3/\kappa$ is the characteristic timescale related to the bending modulus. The external flow strength $S(t) = -S\text{sign}(t - t_0)$, where $S = 16\sqrt{6\pi}\dot{\gamma}\tau/(11\sqrt{5\Delta})$ is a dimensionless value. Following [11], we also define a nondimensional extensional rate $\chi = \dot{\gamma}\tau = \dot{\gamma}\mu R^3/\kappa$, a nondimensional time $\bar{t} = \dot{\gamma}t$, and a nondimensional surface tension $\bar{\sigma} = \sigma R^2/\kappa$. See more details in Appendix B.

Following [29], the equation of motion for each mode is given by

$$\tau \dot{u}_{l,m} = S(t) f_{l,m} - (A_l \sigma + \Gamma_l) u_{l,m}, \quad (11)$$

where $\dot{u}_{l,m}$ is the time derivative of $u_{l,m}(t)$, $f_{l,m} = \delta_{l,2}(\delta_{m,2} + \delta_{m,-2})$, $\delta_{l,m}$ is the Kronecker delta, $\Gamma_l = (l-1)l^2(l+1)^2(l+2)/(4l^3 + 6l^2 - 1)$, and $A_l = l(l+1)(l^2 + l - 2)/(4l^3 + 6l^2 - 1)$. By conservation of the volume and area, i.e., $\partial_t \sum |u_{l,m}|^2 = 0$, the global surface tension reads [29]

$$\sigma = \frac{2S(t)\text{Re}[u_{2,2}] - \bar{\Gamma}}{\bar{A}}, \quad (12)$$

where $\bar{A} = \sum_l A_l \Delta_l$, $\bar{\Gamma} = \sum_l \Gamma_l \Delta_l$, and $\Delta_l = \sum_m |u_{l,m}|^2$.

Combining experimental observations in [28] and analysis of Eqs. (11) and (12), Turitsyn *et al.* [29] find that transient wrinkling dynamics are able to be divided into three stages. In the first stage, the high-order modes grow exponentially after the flow direction is reversed. After saturation of the exponential growth, the second stage starts. The surface tension decays algebraically and the amplitudes for higher modes grow. After reaching the highest wrinkles amplitude, the dynamics finally come to the last stage, where the vesicle evolves to a new stable state with $u_{2,\pm 2} = -1$.

IV. NUMERICAL METHOD

A. Numerical model

We use an immersed boundary method to study the vesicle dynamics numerically [38]. The length scale of experiments and simulations is generally dozens of microns, and the velocity is of the same order, resulting in a low Reynolds number [39]. Therefore, we ignore the nonlinear convection term in the Navier-Stokes equation. One obtains the time-dependent Stokes equation for an incompressible fluid,

$$\rho \frac{\partial \mathbf{u}^{\text{ind}}(\mathbf{x}, t)}{\partial t} = \mu \Delta \mathbf{u}^{\text{ind}}(\mathbf{x}, t) - \nabla p + \mathbf{f}(\mathbf{x}, t), \quad (13)$$

$$\nabla \cdot \mathbf{u}^{\text{ind}}(\mathbf{x}, t) = 0, \quad (14)$$

where ρ is the density of the fluid and $\mathbf{f}(\mathbf{x}, t)$ is the force density acting on the fluid. It is worth noting that Atzberger [39]

also considers thermal fluctuations of the aqueous environment, which will be investigated in the future.

For the typical immersed boundary method, the force density $\mathbf{f}(\mathbf{x}, t)$ acting on the fluid is converted from the force $\mathbf{F}(\mathbf{X}, t)$ associated with the vesicle membrane using a δ function [38,39]. Similarly, the velocity of the vesicle is an interpolation of the velocity for the nearby flow field. By doing so, we get the following fluid-vesicle coupling as

$$\mathbf{f}(\mathbf{x}, t) = \int_S \delta[\mathbf{x} - \mathbf{X}(t)] \mathbf{F}(\mathbf{X}, t) d\mathbf{X}, \quad (15)$$

$$\frac{d\mathbf{X}(t)}{dt} = \int_{\Omega} \delta[\mathbf{x} - \mathbf{X}(t)] \mathbf{u}(\mathbf{x}, t) d\mathbf{x}. \quad (16)$$

B. Discretization

In the immersed boundary method [33,38,39], we use an Eulerian grid to discretize the flow field and a Lagrangian grid to discretize the vesicle. The flow field is a cube with an edge L in all directions. The grid size $\Delta x = L/N$, where N is the number of grid points along each direction. Following [32,33], spatial derivatives in (13) and (14) are approximated by finite-difference schemes,

$$\rho \frac{d\mathbf{u}_m^{\text{ind}}}{dt} = \mu \mathcal{L} \mathbf{u}_m^{\text{ind}} - \mathcal{D} p_m + \mathbf{f}_m, \quad (17)$$

$$\mathcal{D} \cdot \mathbf{u}_m^{\text{ind}} = 0, \quad (18)$$

where $\mathbf{u}_m^{\text{ind}}$, p_m , and \mathbf{f}_m are the velocity, pressure, and force density at the \mathbf{m} th grid point, respectively. Here, $\mathbf{m} = (m_1, m_2, m_3)$ is a vector with integer components. \mathcal{L} is the seven-point discrete Laplacian and \mathcal{D} is the central difference gradient. Thus, the coupled velocity-pressure system is solved on a natural grid.

A discrete fast Fourier transform (FFT),

$$\hat{\mathbf{u}}_{\mathbf{k}}^{\text{ind}} = \frac{1}{N^3} \sum_{\mathbf{m}} \mathbf{u}_m^{\text{ind}} \exp(-i2\pi \mathbf{k} \cdot \mathbf{m}/N), \quad (19)$$

$$\mathbf{u}_m^{\text{ind}} = \sum_{\mathbf{k}} \hat{\mathbf{u}}_{\mathbf{k}}^{\text{ind}} \cdot \exp(i2\pi \mathbf{k} \cdot \mathbf{m}/N), \quad (20)$$

is used in the algorithm. Here each sum runs over N^3 lattice points defined by $0 \leq \mathbf{m}^{(\ell)} \leq N - 1$ and $0 \leq \mathbf{k}^{(\ell)} \leq N - 1$, where the parenthesized superscripts $\ell = 1, 2, 3$ denote the Cartesian components of the indicated vector.

The Stokes equation in Fourier space reads [32,39]

$$\frac{d\hat{\mathbf{u}}_{\mathbf{k}}^{\text{ind}}}{dt} = -\alpha_{\mathbf{k}} \hat{\mathbf{u}}_{\mathbf{k}}^{\text{ind}} - i\rho^{-1} \hat{p}_{\mathbf{k}} \mathbf{g}_{\mathbf{k}} + \rho^{-1} \hat{\mathbf{f}}_{\mathbf{k}}, \quad (21)$$

$$\mathbf{g}_{\mathbf{k}} \cdot \hat{\mathbf{u}}_{\mathbf{k}}^{\text{ind}} = 0, \quad (22)$$

where $\alpha_{\mathbf{k}} = 2\mu/(\rho \Delta x^2) \sum_{j=1}^3 [1 - \cos(2\pi \mathbf{k}^{(j)}/N)]$ and $\mathbf{g}_{\mathbf{k}} = \sin(2\pi \mathbf{k}^{(j)}/N)/\Delta x$. Projecting both sides of Eq. (21) and according to the incompressibility constraint (22), one obtains $\hat{p}_{\mathbf{k}}(t) = -i\mathbf{g}_{\mathbf{k}} \cdot \hat{\mathbf{u}}_{\mathbf{k}}^{\text{ind}}/|\mathbf{g}_{\mathbf{k}}|^2$. Equation (21) is simplified into a linear differential equation with one unknown. The recurrence equation of $\hat{\mathbf{u}}_{\mathbf{k}}^{\text{ind}}$ at discrete time $t_n = n\Delta t$ is then given as [32,39]

$$\hat{\mathbf{u}}_{\mathbf{k}}^{\text{ind},n+1} = e^{-\alpha_{\mathbf{k}} \Delta t} \hat{\mathbf{u}}_{\mathbf{k}}^{\text{ind},n} + \frac{(1 - e^{-\alpha_{\mathbf{k}} \Delta t})}{\rho \alpha_{\mathbf{k}}} \xi_{\mathbf{k}} \hat{\mathbf{f}}_{\mathbf{k}}^n, \quad (23)$$

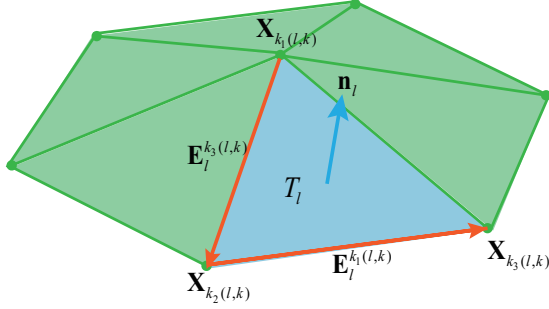


FIG. 2. Illustration of the triangular mesh model.

where $\hat{\mathbf{u}}_{\mathbf{k}}^{\text{ind},n} = \hat{\mathbf{u}}_{\mathbf{k}}^{\text{ind}}(t_n)$, $\hat{\mathbf{f}}_{\mathbf{k}}^n = \hat{\mathbf{f}}_{\mathbf{k}}(t_n)$, and $\xi_{\mathbf{k}} = I - \mathbf{g}_{\mathbf{k}} \cdot \mathbf{g}_{\mathbf{k}}^T / |\mathbf{g}_{\mathbf{k}}|^2$. On the other hand, the time derivative in Eq. (21) can be approximated by the forward Euler, which is simpler than Eq. (23). The forward Euler gives the same results as that obtained by Eq. (23). However, the recurrence equation (23) is more robust and can be extended to investigate dynamics under thermal fluctuations. Considering the extensibility of the method and the program, we use the format (23).

The vesicle is discretized by a triangular mesh with edge $a \approx 2\Delta x$ and a total number of vertices M [40]. Following [33], let \mathbf{X}_k , i.e., $\mathbf{X}_{k_1(l,k)}$ in Fig. 2, be the position of the k th mesh point. The curvature vector at the vertex \mathbf{X}_k is defined as

$$\mathbf{H}^{(k)} = -\frac{1}{2} \sum_{l \in \mathcal{T}(k)} \mathbf{n}_l \times \mathbf{E}_l^k, \quad (24)$$

where $\mathcal{T}(k)$ is the set of triangles containing \mathbf{X}_k , \mathbf{n}_l is the unit normal of the l th triangle T_l pointing outside, and \mathbf{E}_l^k is the edge vector in triangle T_l opposite to \mathbf{X}_k . See Appendix A for more detailed mathematical symbols in Fig. 2. The total discrete bending energy then reads

$$\mathbf{E}_b = \frac{\kappa}{2} \sum_{k=1}^M \frac{\|\mathbf{H}^{(k)}\|^2}{A^{(k)}}. \quad (25)$$

Here, $A^{(k)} = \frac{1}{3} \sum_{l \in \mathcal{T}(k)} A_l$ is the area associated with the vertex \mathbf{X}_k , where A_l is the area of T_l . Using a variational approach, we get the discretized elastic force $\mathbf{F}_b(\mathbf{X}_k)$ and local surface tension $\mathbf{F}_\sigma(\mathbf{X}_k)$ at each mesh point. See Appendix A for details.

In the immersed boundary method, the Eulerian and Lagrangian variables are linked by a Dirac δ function [38], which is given by

$$\delta_a(\mathbf{r}) = \frac{1}{a^3} \phi\left(\frac{r_1}{a}\right) \phi\left(\frac{r_2}{a}\right) \phi\left(\frac{r_3}{a}\right), \quad (26)$$

for any $\mathbf{r} = (r_1, r_2, r_3) \in \mathbb{R}^3$, where $\phi(r)$ is given by

$$\phi(r) = \begin{cases} \frac{1}{8}(3 - 2|r| + \sqrt{4|r| + 1 - 4r^2}), & |r| \leq 1 \\ \frac{1}{8}(5 - 2|r| - \sqrt{12|r| - 7 - 4r^2}), & 1 < |r| \leq 2 \\ 0, & |r| > 2. \end{cases} \quad (27)$$

Then the force density acting on the fluid is given as

$$\mathbf{f}_{\mathbf{m}}^n = \sum_{k=1}^M \mathbf{F}(\mathbf{X}_k^n) \delta_a(\mathbf{x}_{\mathbf{m}} - \mathbf{X}_k^n). \quad (28)$$

TABLE I. The relative error for the vesicle.

Steps	10 000	100 000	1 000 000
$\max(\mathcal{E}_{\mathbf{X}_k})$	1.24×10^{-5}	1.12×10^{-4}	1.34×10^{-3}
$\max(\mathcal{E}_{\mathbf{u}_k^{\text{ind}}})$	1.11×10^{-2}	1.15×10^{-2}	1.56×10^{-2}

The time discretization for Eq. (16) is developed by integrating the induced fluid velocity field over a time step,

$$\mathbf{X}_k^{n+1} = \mathbf{X}_k^n + \sum_{\mathbf{m}} \delta_a(\mathbf{x}_{\mathbf{m}} - \mathbf{X}_k^n) \Gamma_{\mathbf{m}}^n \Delta x^3 + \mathbf{u}^\infty(\mathbf{X}_k^n) \Delta t, \quad (29)$$

where $\Gamma_{\mathbf{m}}^n = \int_{t_n}^{t_{n+1}} \mathbf{u}_{\mathbf{m}}^{\text{ind}}(s) ds$. According to the properties of the Fourier transform, this time integral is calculated by expression (23) for the Fourier modes of the induced fluid velocity field [39],

$$\begin{aligned} \Gamma_{\mathbf{m}}^n &= \sum_{\mathbf{k}} \hat{\Gamma}_{\mathbf{k}}^n \exp(i2\pi \mathbf{k} \cdot \mathbf{m}/N), \\ \hat{\Gamma}_{\mathbf{k}}^n &= \int_{t_n}^{t_{n+1}} \hat{\mathbf{u}}_{\mathbf{k}}^{\text{ind}}(s) ds, \\ &= -\frac{e^{-\alpha_{\mathbf{k}} \Delta t} - 1}{\alpha_{\mathbf{k}}} \hat{\mathbf{u}}_{\mathbf{k}}^{\text{ind},n} + \frac{\alpha_{\mathbf{k}} \Delta t + e^{-\alpha_{\mathbf{k}} \Delta t} - 1}{\rho \alpha_{\mathbf{k}}^2} \xi_{\mathbf{k}} \hat{\mathbf{f}}_{\mathbf{k}}^n. \end{aligned}$$

Note that $\Gamma_{\mathbf{m}}^n$ is solved under the periodic boundary condition, while \mathbf{u}^∞ is not. Following [32,41], we test the influence of the periodic boundary condition on the vesicle. We increase the domain size L , which initially is $L \approx 2.5l_0$ where l_0 is the diameter of the vesicle. We keep all other parameters the same and rerun the simulation. The maximum relative errors of the membrane velocity and the membrane shape are shown in Table I. Those results show that the periodic boundary condition has little effect on the shape of the vesicle, given $L \geq 2.5l_0$. Also, note that $\mathcal{E}_{\mathbf{X}_k}$ is significantly smaller than $\mathcal{E}_{\mathbf{u}_k^{\text{ind}}}$ and the maximum of $\mathcal{E}_{\mathbf{u}_k^{\text{ind}}}$ usually occurs when $|\mathbf{u}_k^{\text{ind}}|$ is small.

According to the algorithm in [33] and [39], we write our program and use a GPU paralleling strategy to accelerate the simulation. The FFT solving \mathbf{u}^{ind} consumes up to 90% of computing time. It is extremely efficient to use GPU parallelization because the bottleneck of the FFT algorithm is the memory bandwidth, given sufficient cores. All the parallel computations carried out with the aid of CUDA C [42] are done on a single Nvidia V100 GPU with 32 GB memory and 900 GB/second bandwidth. We use AMD Ryzen 7 5800H to test the performance of the same scheme that runs in MATLAB on the CPU, as a reference. The results are shown in Table II. The GPU parallelization accelerates the simulation by at least two orders of magnitude.

TABLE II. A comparison of the computational time among CPU algorithm and GPU parallelization at 1 step and 1 s ($\Delta t = 10^{-7}$ s).

Nx	GPU		CPU		Ratio
	1 step	1 s (est.)	1 step	1 s (est.)	
128	0.0024 s	7 h	0.43 s	2 months	183
256	0.0173 s	2 days	1.82 s	7 months	105
512	0.1329 s	15 days	22.57 s	7 years	170

TABLE III. System parameters.

Parameters	Description	Value
T	Temperature	293 K
L	Domain length in each direction	9×10^{-5} m
ρ	Uniform density of fluid	1000 kg/m^3
μ	Dynamic viscosity of fluid	1.435×10^{-3} Pa s
κ	Bending modulus	1×10^{-19} J
Δt	Time step	1×10^{-7} s
Δx	Mesh width of fluid	1.7578×10^{-7} m

V. RESULTS AND DISCUSSION

We use the same parameters as in the experiments [28], shown in Table III. The domain of the fluid is a cube of 512^3 nodes. The equivalent radii of quasispherical vesicles and elliptical vesicles used in the simulations are $R = 1.671 \times 10^{-5}$ m and $R = 1.8 \times 10^{-5}$ m, respectively. The extensional rates of the weak and strong flows are $\dot{\gamma} = 1 \text{ s}^{-1}$ and $\dot{\gamma} = 4 \text{ s}^{-1}$, respectively.

A. Comparison with perturbation analysis

We compare the numerical results of global surface tension σ , $\Delta_2 = \sum_m |u_{2,m}|^2$ and the characteristic Δ_{l_*} with predictions of the perturbation analysis. Δ_l represents the amplitude of wrinkles for the l -order mode. When the membrane surface is smooth, most of the excess area is stored in $\Delta_2(t)$. When $\Delta_2(t)$ reaches its minimum at t_* , the amplitude of wrinkles is the highest. At t_* , $\Delta_{l_*}(t_*) \geq \Delta_l(t_*)$ ($2 \leq l \leq l_{\max}$), where l_{\max} is the largest nontrivial mode with $|u_{l,m}| > 10^{-5}$. Given l_* , the l_* -order spectral distribution evolves according to $\Delta_{l_*}(t) = \sum_{m=-l_*}^{l_*} |u_{l_*,m}(t)|^2$.

1. Wrinkling dynamics for a quasispherical vesicle

We set the vesicle to be an ellipsoid with aspect ratio $x : y : z = 1 : 0.8 : 1$, i.e., $\Delta = 0.116$. For the weak extensional flow, $\dot{\gamma} = 1 \text{ s}^{-1}$, $\chi = 67$, and $S = 553$. For the strong extensional flow, $\dot{\gamma} = 4 \text{ s}^{-1}$, $\chi = 268$, and $S = 2224$. The triangular mesh of the vesicle is composed of 26 070 vertices and 52 136 triangles.

We first solve Eqs. (11) and (12) numerically using the Euler method. The initial distribution is $|u_{l,m}|^2 \sim 2k_B T / \kappa (l^4 + Sl^2/A_2)$ [29], where k_B is the Boltzmann constant. One obtains the evolution of global surface tension $\sigma(t)$ and the amplitude of each mode in the spherical harmonics $u_{l,m}(t)$ from perturbation analysis.

Next, for the vesicle in simulation, we use spherical harmonics expansion to investigate its shape at time t . We set $\mathbf{X}_i^c(t)$ to be the geometric center for the i th triangle at time t . The spherical coordinate $[r_i(t), \theta_i(t), \phi_i(t)]$ is calculated through the vector $\mathbf{X}_i^c(t) - \mathbf{X}_C(t)$, where $\mathbf{X}_C(t)$ is the geometric center of the whole vesicle. The amplitude for each mode is then computed as

$$u_{l,m}(t) = \sqrt{\frac{(l-1)(l+2)}{\Delta}} \sum_{i=1}^M \frac{r_i(t) - R}{R} Y_{l,m}(\theta_i, \phi_i) \Delta \Omega_i, \quad (30)$$

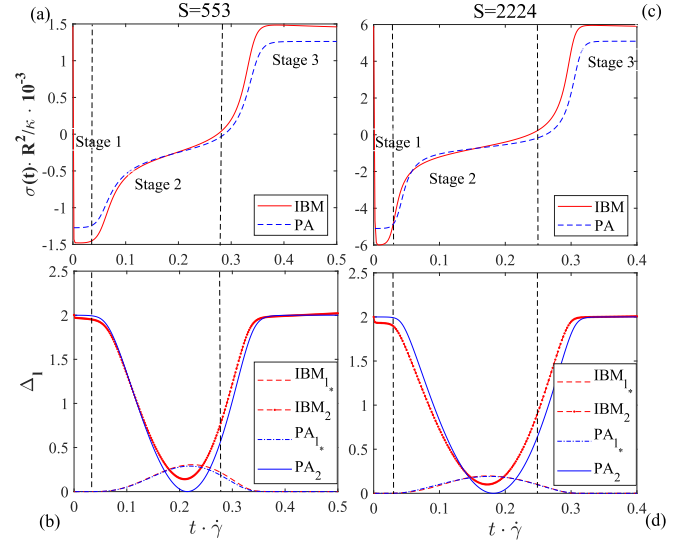


FIG. 3. Wrinkling dynamics of a quasispherical vesicle from the immersed boundary method (IBM) and perturbation analysis (PA). (a) and (c) show the evolution of dimensionless $\sigma(t)$; (b) and (d) show the evolution of Δ_2 and Δ_{l_*} , for flow strength $S = 553$ and 2224 , respectively. In the weak flow ($S = 553$) and the strong flow ($S = 2224$), perturbation analysis predicts the characteristic wrinkle wavelength $l_* = 14$ and $l_* = 25$, while simulation results show $l_* = 15$ and $l_* = 28$, respectively. The timescale starts with t_0 .

where $\Delta \Omega_i = A_i / r_i^2$ is the integral element that approximates $\sin \theta d\theta d\phi$.

As shown in Fig. 3, our numerical results agree with the perturbation analysis. Figures 3(a) and 3(c) compare the evolution of $\sigma(t)$. Figures 3(b) and 3(d) compare Δ_2 and Δ_{l_*} . When $S = 553$ and $S = 2224$, perturbation analysis predicts the characteristic wrinkle mode $l_* = 14$ and $l_* = 25$, while numerical results produce $l_* = 15$ and $l_* = 28$, respectively. A possible reason for this discrepancy is that the effective excess area, characterized by the change in Δ_2 , is less in nonlinear simulations. The minimum value of Δ_2 by IBM is close but not equal to 0, as shown in Figs. 3(b) and 3(d).

We mark the three evolution stages along the curve in Fig. 3. During the first stage, the global surface tension is almost constant and most of the excess area is stored in the second-order angular harmonics. The high-order harmonics grow exponentially following the equation $u_{l,m}(t) = u_{l,m}(0) \exp(-\Gamma_l t / \tau + A_l \zeta)$, where $\zeta = -\int_0^t \sigma(t') / \tau dt'$ is the solution of the equation $\tau d\zeta / dt = -\sigma$ [29]. The second stage starts after the exponential growth has saturated. The numerical global surface tension decays algebraically as $\sigma(t) \sim t^{-0.7439}$ and $\sigma(t) \sim t^{-0.8108}$ for $S = 553$ and $S = 2224$, respectively. The $|u_{l,m}(t)|$ for high-order modes are still increasing. During the third stage, $\sigma(t)$ recovers its equilibrium value. We further explore the relationship between the characteristic wrinkle wavelength l_* and the flow strength S . The wavelength l_* is calculated in the same way as k_* in Ref. [28],

$$l_* = \sqrt{\frac{\sum_{3 \leq l \leq l_{\max}} l^2 / (l^2 + l - 2) \sum_{-l \leq m \leq l} u_{l,m}^2}{\sum_{3 \leq l \leq l_{\max}} 1 / (l^2 + l - 2) \sum_{-l \leq m \leq l} u_{l,m}^2}}. \quad (31)$$

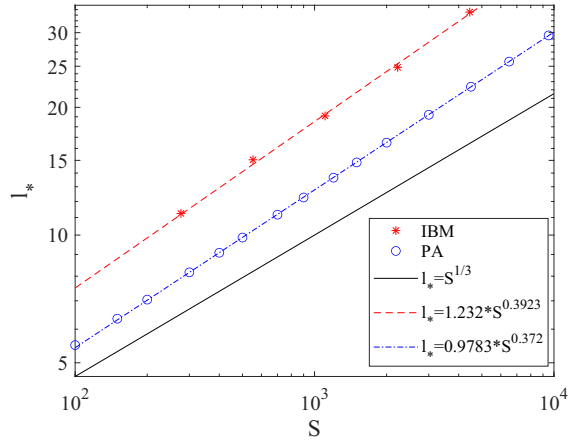


FIG. 4. The relationship between the characteristic wrinkle wavelength l_* and the flow strength S is shown in a log-log scale.

The theoretical results are given under 15 flows of S from 100 to 9500. In the simulation, l_* is obtained under five flows with $S = 227, 553, 1106.5, 2224, \text{ and } 4448$. The relationship between l_* and S in the log-log scale is presented in Fig. 4. The perturbation analysis l_* obeys the function $l_* \sim S^{0.372}$. It is in good agreement with the numerical result $l_* \sim S^{0.3923}$. The slope of the fitting curve is also in reasonable agreement with the conclusion $l_* \sim S^{1/3}$ given in [29].

2. Wrinkling dynamics for an ellipsoidal vesicle

We study the wrinkling dynamics of ellipsoidal vesicles with $\Delta = 0.997$. As shown in Fig. 5, we plot results for an ellipsoidal vesicle in the weak flow $S = 237$ ($\chi = 83.5$) and the strong flow $S = 947$ ($\chi = 335$). The minimum value of

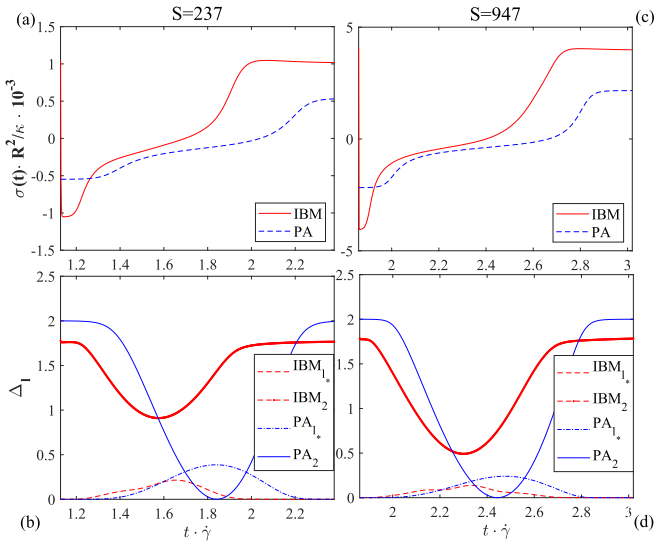


FIG. 5. Comparison with perturbation analysis. Evolution of the global surface tension with $\Delta = 0.9972$ in (a) weak flow $\chi = 83.5$, $S = 237$ and (c) strong flow $\chi = 4$, $S = 947$. (b) and (d) show Δ_2 and Δ_1 . When $S = 237$ and $S = 947$, perturbation analysis predicts $l_* = 10$ and $l_* = 17$, while the simulation results show $l_* = 12$ and $l_* = 24$, respectively.

Δ_2 for nonlinear simulations is always away from 0, which means the effective excess area is smaller than the perturbation analysis. The effective excess area is larger in a strong flow. Note that the global surface tension is larger and the relaxation time is shorter in numerical simulations. We also study ellipsoidal vesicles with $\Delta = 1.65$ and get similar results. These discrepancies imply that nonlinear effects are significant for off-spherical vesicles.

B. Comparison with experiments

We explore two wrinkling dynamics which are observed in the experiments [28]. Comparison between numerical and experimental results are shown in Fig. 6. After the external flow is reversed, the vesicle membrane produces high-frequency disturbances driven by negative surface tension, as shown in Figs. 6(a) and 6(c). In both strong and weak flow, the extrusion and stretching processes of the simulations are almost the same as that observed in the experiments. Yet, our simulations clearly capture much richer details. The vesicle finally retains a stable ellipsoidal shape aligning with the new external flow, in agreement with Ref. [43]. Figure 6(e) shows the detail of vesicle wrinkles from different angles. At $\bar{t} = 2.33$, we plot the shape of the wrinkled membrane from the front, back, left, right, top, and bottom points of view. The back direction is the angle of view in Fig. 6(c).

As shown in Fig. 6, a numerical study is beneficial and necessary for comprehending the wrinkling phenomenon of vesicles. In 2D experimental snapshots, one could not fully understand the exact shape of the vesicle, even the number and size of wrinkles. For example, as shown in Fig. 6(b) at $\bar{t} = 1.46$, on the left side of the vesicle, one might wonder what the shadow area near the three protrusions indicates. On the other hand, there are two depressions at this part in Fig. 6(a) at $\bar{t} = 1.46$. These are two troughs, if we describe wrinkles as waves (wrinkles are described as waves in following paragraphs for convenience). Our findings are helpful in understanding the experimental results. Comparing Figs. 6(c), 6(d), and 6(e), we find that the vesicle wrinkle reduction stage might not be as smooth as the experimental snapshots show. The edge is sharp and there are many depressions and protuberances evolved around the middle, which can hardly be imagined in Fig. 6(d).

Compared with 2D simulations, much more detailed morphological information about wrinkles is obtained from 3D simulations. Figure 6(e) shows that wrinkles are concentrated around the axial vertex of the ellipsoid along the elongational axis direction, while there are fewer wrinkles on other sides. Similar facts are observed in both 2D simulations and experimental snapshots, but are not as adequate and precise. According to [34,35], wrinkles are described as highly disordered zigzag herringbone patterns and tend to be peanut shaped for the strong flow (see Appendix C and Ref. [34] for more details).

C. Properties of wrinkling dynamics

The local surface tension is calculated on each triangle of the membrane mesh according to Appendix A 2, but not on nodes. The global surface tension is obtained by averaging

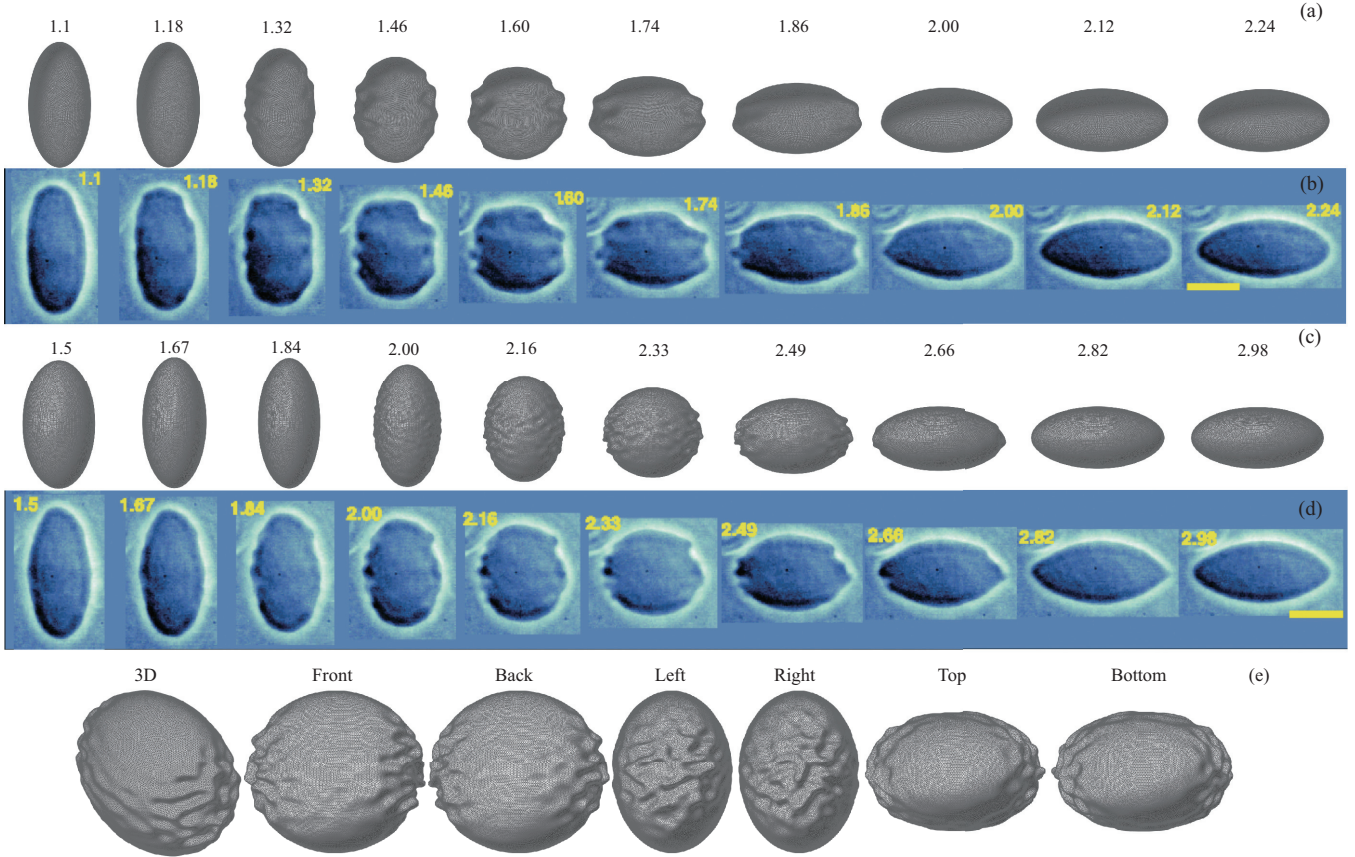


FIG. 6. Comparison with experiments. The wrinkling dynamics in time-dependent extensional flow at (b) $\chi = 81$, (d) $\chi = 323.5$ are taken from Fig. 2 of Kantsler *et al.* [28]. The simulated wrinkling dynamics of the vesicle are shown in (a) $\chi = 83.5$, $S = 237$ and (c) $\chi = 335$, $S = 947$, where numbers are $\bar{t} = \dot{\gamma}t$. (e) Wrinkling of a vesicle in extension flow $\chi = 335$, at $\bar{t} = 2.33$. The front and back are the views of the two opposite directions along the z axis. The left and right are the views of the two opposite directions along the y axis. The top and bottom are the views of the two opposite directions along the x axis.

all the local surface tension. In Figs. 5(a) and 5(b), we plot the evolution of the global surface for wrinkling dynamics of the vesicle with $\Delta = 0.997$ and $S = 237, 947$, respectively. The corresponding local surface tension is shown in Figs. 7(a) and 7(b). We also present the corresponding detailed local surface tension of the vesicle in Fig. 6(e), as illustrated in Fig. 7(c).

As shown in Figs. 5(a) and 5(c), the global surface tension quickly changes from positive to negative after the external flow is suddenly reversed. Then it gradually increases until reaching the same positive value, which represents a new equilibrium state. Changes in surface tension correspond to the generation, growth, and decay of wrinkles. Figure 7 shows that the local surface tension varies significantly along the vesicle, and the inhomogeneous local surface tension causes the irregularity of wrinkles on the membrane.

Quantitative analysis is performed with the help of spherical harmonics. Using the least-squares method, the vesicle surface is fitted by an ellipsoid. The amplitude $A_p(\theta, \phi; \bar{t})$, i.e., the deviation from the fitted ellipsoid, is taken as a function of ϕ and θ for each time step. Examples of $A_p(\theta, \phi; \bar{t})$ are shown in Figs. 8(a) and 8(b). These figures clearly show that wrinkles are mainly concentrated near the points $\theta = \frac{\pi}{2}$, $\phi = \pm \frac{\pi}{2}$, i.e., the intersections of the y axis and the membrane, and tend to converge towards the y axis. This trend is not seen in [28]

and [29]. We use

$$\bar{A}_p(\bar{t}) = \frac{1}{A} \sum_{i \in T} A_p^2(\theta_i, \phi_i; \bar{t}) A_i$$

to quantify the magnitude of the wrinkling behavior, as shown in Figs. 8(d) and 8(e). The results show precisely when the process begins. The maximum value of the amplitude is larger in the weak flow, which indicates less excited high-order modes.

The spherical harmonics expansion of the amplitude is $A_p(\theta, \phi) = R \sum_{l \geq 0}^l \sum_{m=-l}^l \tilde{u}_{l,m} Y_{l,m}(\theta, \phi)$. The coefficient is calculated as

$$\tilde{u}_{l,m}(\bar{t}) = \sum_{i=1}^M \frac{A_p(\theta_i, \phi_i; \bar{t})}{R} Y_{l,m}(\theta_i, \phi_i) \Delta \Omega_i. \quad (32)$$

An example of $\tilde{u}_{l,m}(\bar{t})$ is shown in Fig. 8(c). Higher-order modes are also excited at $\bar{t} = 2$ and 2.33. For the same l , $\tilde{u}_{l,m}(\bar{t})$ is large for only a few m . High-order modes are quasisymmetric for $m = 0$. These results agree with Figs. 8(a) and 8(b), where the amplitudes are also quasisymmetric with respect to $\theta = \pi/2$. One possible reason is that the two-dimensional external flow ($u_x^\infty = \dot{\gamma}x$, $u_y^\infty = -\dot{\gamma}y$, but $u_z^\infty = 0$) induces “two-dimensional” wrinkles. Therefore, 2D simulations are able to capture many important features.

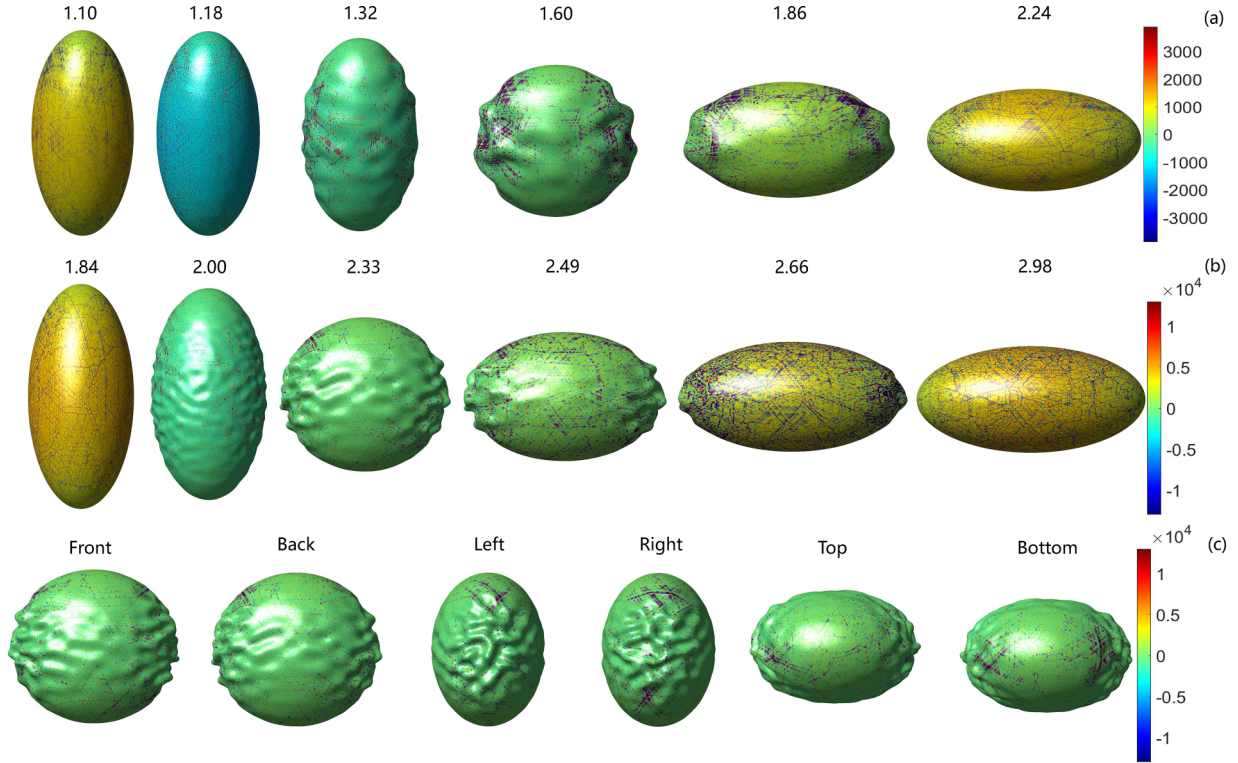


FIG. 7. The local surface tension of vesicles in extensional flow with (a) $\chi = 83.5, S = 237$, (b) $\chi = 335, S = 947$ (values in color); numbers are $\dot{\gamma}t$. (c) From the front, back, left, right, top, and bottom view, local surface tension of the vesicle as shown in (b) at $\dot{\gamma}t = 2.33$ (values in color).

In Figs. 8(f) and 8(g), we plot the distribution of excess area $\tilde{\Delta}_l(\bar{t}) = \sum_m |\tilde{u}_{l,m}(\bar{t})|^2$ as a function of time and l . Even-order modes are more excited due to the symmetry of the shape of the vesicle and the flow field. Also, the diagrams clearly show that more high-order modes are excited for the strong flow, which is consistent with [28].

VI. CONCLUSION

The main goal of the current study is to explore the wrinkling dynamics of 3D vesicles in a time-dependent elongation flow. We have simulated the dynamics of 3D vesicle wrinkling observed in the experiment [28] utilizing the immersed boundary method. Our results suggest more accurate detailed information and explanation of experimental snapshots. We also obtain information about wrinkle patterns that are not approached in 2D simulations. 3D simulations of quasispherical vesicles match well with the perturbation analysis predictions. We have proposed a quantified relationship between the characteristic wrinkle wavelength and the flow strength $L_* \sim S^{0.3923}$. But there are some discrepancies in the elongated vesicle dynamics between simulations and perturbation analysis, highlighting the importance of nonlinear effects. Thus, we have investigated an efficient and accurate numerical to solve a fluid-structure interaction problem. Using a spherical harmonic function to parametrize the vesicle profile, we have analyzed the mode of vesicle wrinkling dynamics. Not only are low-order modes excited, but many high-order modes are also excited. Even-order modes excite more obviously than odd-order modes. For the same l , $\tilde{u}_{l,m}(\bar{t})$ is large for only a few

m . The wrinkle amplitudes are quasisymmetric to $\theta = \pi/2$. The excited high-order modes are quasisymmetric to $m = 0$. The inhomogeneous local surface tension causes the irregularity of wrinkles on the vesicle membrane. A stronger flow excites larger surface tension and more high-order modes. Accordingly, we have observed smaller wrinkle amplitudes.

It is interesting to note that our methods and studies are favorable to the simulation of dynamics in a broad class of applications arising in technological systems and biology [2,3]. Since specific information about wrinkle patterns can be obtained in 3D simulations, we are able to conveniently and concretely study the relationship between various factors, such as external field intensity, vesicle shape, and wrinkle morphology. In turn, vesicle morphology can be applied to many applications, including diffraction gratings, stretchable electronics, cell adhesion and growth, and antifouling [34]. Although we focus on the 3D simulation of the ellipsoidal vesicle in extensional flow, the numerical methods are universal and can be swimmingly applied to other vesicles and viscous fluids. Moreover, thermal noise is an influential factor affecting vesicle wrinkling dynamics [8,31]. We plan to study the effect of thermal noise on the vesicle.

ACKNOWLEDGMENTS

We are grateful to the anonymous referees for useful comments and suggestions. This research is supported by the Fundamental Research Funds for the Central Universities, HUST: No. 2021JYCXJJ013 and No. 2022JYCXJJ058.

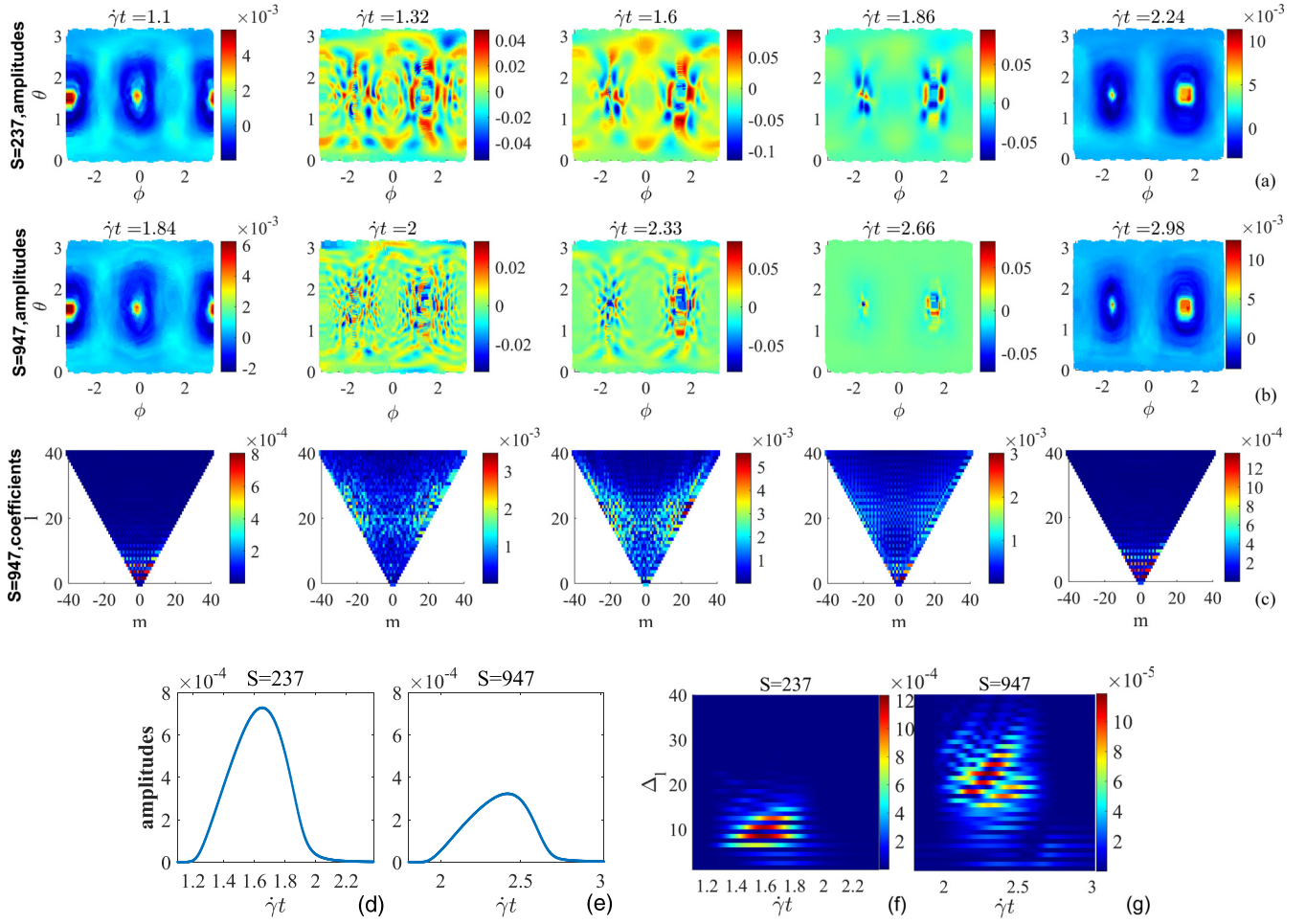


FIG. 8. Quantitative analysis of the wrinkle dynamics. Amplitudes $A_p(\theta, \phi; \bar{t})$ of the higher harmonics vs θ and ϕ at certain times for (a) $S = 237$ and (b) $S = 947$ (values in color). (c) The spherical harmonics coefficient $|\tilde{u}_{l,m}(\bar{t})|$ of amplitudes at certain times for $S = 947$ (values in color). The average amplitude of the higher harmonics with respect to \bar{t} for (d) $S = 237$ and (e) $S = 947$. (f) and (g) show the temporal evolution of excess area $\tilde{\Delta}_l(\bar{t}) = \sum_m |\tilde{u}_{l,m}(\bar{t})|^2$ (values in color).

APPENDIX A: DISCRETIZATION OF THE VESICLE

We discretize energies of (1) and (2), and compute forces in this Appendix which is closely related to Ref. [33].

We first introduce some necessary mathematical symbols. Let $\mathbf{X}_{k_1(l,k)}$ be the vertex \mathbf{X}_k in the l th triangle T_l . The next vertex of $\mathbf{X}_{k_1(l,k)}$ is $\mathbf{X}_{k_2(l,k)}$ and the next vertex of $\mathbf{X}_{k_2(l,k)}$ is $\mathbf{X}_{k_3(l,k)}$ in triangle T_l . The vertices are in counterclockwise order when viewed from outside the vesicle, as shown in Fig. 2. The edge vector of triangle T_l opposite to the vertex $\mathbf{X}_{k_1(l,k)}$ is $\mathbf{E}_l^{k_1(l,k)} = \mathbf{X}_{k_3(l,k)} - \mathbf{X}_{k_2(l,k)}$.

Thus, the unit normal of the triangle T_l can be computed as

$$\begin{aligned} \mathbf{n}_l &= \frac{(\mathbf{X}_{k_2(l,k)} - \mathbf{X}_{k_1(l,k)}) \times (\mathbf{X}_{k_3(l,k)} - \mathbf{X}_{k_1(l,k)})}{\|(\mathbf{X}_{k_2(l,k)} - \mathbf{X}_{k_1(l,k)}) \times (\mathbf{X}_{k_3(l,k)} - \mathbf{X}_{k_1(l,k)})\|} \\ &= \frac{\mathbf{E}_l^{k_3(l,k)} \times \mathbf{E}_l^{k_2(l,k)}}{\|\mathbf{E}_l^{k_3(l,k)} \times \mathbf{E}_l^{k_2(l,k)}\|}. \end{aligned} \quad (\text{A1})$$

The area of T_l is $A_l = \frac{1}{2} \mathbf{n}_l \cdot (\mathbf{E}_l^{k_2(l,k)} \times \mathbf{E}_l^{k_3(l,k)})$. In addition, let $\mathcal{V}(l)$ be a set of indices of vertices in triangle T_l and $\mathcal{N}(k)$ be a set of indices of all neighboring vertices that are connected to \mathbf{X}_k .

1. Bending forces

The bending force at \mathbf{X}_k is deduced by (25),

$$\begin{aligned} \mathbf{F}_b(\mathbf{X}_k) &= -\frac{\partial \mathbf{E}_b}{\partial \mathbf{X}_k} = -\frac{\partial}{\partial \mathbf{X}_k} \left(\frac{\kappa}{2} \sum_{j=1}^M \frac{\|\mathbf{H}^{(j)}\|^2}{A^{(j)}} \right) \\ &= -\frac{\kappa}{2} \left(\frac{\partial}{\partial \mathbf{X}_k} \frac{\|\mathbf{H}^{(k)}\|^2}{A^{(k)}} + \sum_{k' \in \mathcal{N}(k)} \frac{\partial}{\partial \mathbf{X}_k} \frac{\|\mathbf{H}^{(k')}\|^2}{A^{(k')}} \right). \end{aligned} \quad (\text{A2})$$

We use the chain rule and the triple vector product algebraic rules to simplify the above partial derivatives. Then we rearrange terms so that they are organized by triangles instead of vertices and obtain the bending force,

$$\begin{aligned} \mathbf{F}_b(\mathbf{X}_k) &= \frac{\kappa}{2} \sum_{l \in \mathcal{T}(k)} \left[(\bar{H}_l - \mathbf{n}_l \cdot \mathbf{C}_l) \left(\frac{1}{2} \mathbf{n}_l \times \mathbf{E}_l^k \right) \right] \\ &\quad + \frac{\kappa}{2} \sum_{l \in \mathcal{T}(k)} \left(\frac{1}{2} \mathbf{C}_l \times \mathbf{E}_l^k + \mathbf{n}_l \times \mathbf{h}_l^k \right), \end{aligned} \quad (\text{A3})$$

where

$$\begin{cases} \bar{H}_l = \frac{1}{3} \sum_{p \in \mathcal{V}(l)} \frac{\|\mathbf{H}^{(p)}\|^2}{(A^{(p)})^2}, \\ \mathbf{C}_l = \frac{1}{A_l} \sum_{p \in \mathcal{V}(l)} \mathbf{E}_l^p \times \frac{\mathbf{H}^{(p)}}{A^{(p)}}, \\ \mathbf{h}_l^k = \frac{\mathbf{H}^{[k_3(l,k)]}}{A^{[k_3(l,k)]}} - \frac{\mathbf{H}^{[k_2(l,k)]}}{A^{[k_2(l,k)]}}. \end{cases} \quad (\text{A4})$$

That is, we compute the bending force only using the morphological information about the vesicle. The complete derivation of this formula is shown in Appendix A of Ref. [33].

2. Surface tension forces

Numerically, we consider the surface tension energy mentioned in Ref. [33],

$$\mathbf{E}_\sigma = \int_S \frac{1}{2} \wedge \left(\frac{dA - dA_0}{dA_0} \right)^2 dA_0, \quad (\text{A5})$$

where \wedge equals the surface tension at every point of the membrane. We remark that this is still not realistic enough for a lipid bilayer, which resists local change in area more strongly. This surface tension \wedge is about two orders of magnitude larger than the surface tension of real lipid membranes, reported by Rawicz [44]. The reason that we use this simple surface tension model is that the simulation is able to be compared with the perturbation analysis.

Deriving a discrete surface tension force from (A5) is very complicated. Considering the computational cost, we take the numerical approximation of the surface tension forces,

$$\begin{aligned} \mathbf{F}_\sigma(\mathbf{X}_k) \approx & \beta \frac{\wedge}{A_l} (\mathbf{E}_l^k \cdot \mathbf{E}_l^{k_3(l,k)}) \mathbf{E}_l^{k_2(l,k)} \\ & - \beta \frac{\wedge}{A_l} (\mathbf{E}_l^k \cdot \mathbf{E}_l^{k_2(l,k)}) \mathbf{E}_l^{k_3(l,k)}, \end{aligned} \quad (\text{A6})$$

where $\beta = (A_l - A_l^0)/A_l^0$ and A_l^0 is the initial area of T_l . The dimensionless initial surface tensions $\bar{\wedge} = \wedge R^2/\kappa$ of quasi-spherical vesicles used in weak flow and strong flow are 6×10^{10} and 4.8×10^{11} , respectively. The $\bar{\wedge}$ of elliptical vesicles used in weak flow and strong flow are 2.9×10^{10} and 2.31×10^{11} , respectively. The theoretical surface tension force and the numerical surface tension force are the same because we must have a force balance between the hydrodynamic force and elastic force at the vesicle membrane [45]. We divide \mathbf{F}_σ by the perimeter of the small triangle on the membrane to obtain a new numerical local surface tension σ . This surface tension has the same physics as the theoretical surface tension in Eq. (2).

Finally, we obtain the total forces at \mathbf{X}_k ,

$$\mathbf{F}(\mathbf{X}_k^n) = \mathbf{F}_b(\mathbf{X}_k^n) + \mathbf{F}_\sigma(\mathbf{X}_k^n). \quad (\text{A7})$$

APPENDIX B: NONDIMENSIONALIZATION

We take nondimensional space $\bar{\mathbf{x}} = \mathbf{x}/R$ and time $\bar{t} = \dot{\gamma}t$. Then the nondimensional immersed boundary equations are written as

$$\text{Re} \frac{\partial \bar{\mathbf{u}}^{\text{ind}}}{\partial \bar{t}} = \bar{\nabla}^2 \bar{\mathbf{u}}^{\text{ind}} - \bar{\nabla} \bar{p} + \chi \bar{\mathbf{f}}, \quad (\text{B1})$$

$$\bar{\nabla} \cdot \bar{\mathbf{u}}^{\text{ind}} = 0, \quad (\text{B2})$$

$$\bar{\mathbf{f}} = \int_S \bar{\delta}[\bar{\mathbf{x}} - \bar{\mathbf{X}}(\bar{t})] \bar{\mathbf{F}}(\bar{\mathbf{X}}, \bar{t}) d\bar{\mathbf{X}}, \quad (\text{B3})$$

$$\frac{d\bar{\mathbf{X}}(\bar{t})}{d\bar{t}} = \int_{\bar{\Omega}} \bar{\delta}[\bar{\mathbf{x}} - \bar{\mathbf{X}}(\bar{t})] \bar{\mathbf{u}}(\bar{\mathbf{x}}, \bar{t}) d\bar{\mathbf{x}}. \quad (\text{B4})$$

Here, $\text{Re} = \dot{\gamma} \rho R^2/\mu$ is the Reynolds number. The nondimensional velocity $\bar{\mathbf{u}}^{\text{ind}} = \mathbf{u}^{\text{ind}}/(\dot{\gamma}R)$, $\bar{\mathbf{u}}_{\bar{x}}^\infty = \bar{x}$, $\bar{\mathbf{u}}_{\bar{y}}^\infty = -\bar{y}$, and $\bar{\mathbf{u}}_{\bar{z}}^\infty = 0$. The nondimensional pressure $\bar{p} = p/(\mu\dot{\gamma})$, $\bar{\mathbf{F}}(\bar{\mathbf{X}}, \bar{t}) = \mathbf{F}(\mathbf{X}, t)R/\kappa$, $\bar{A} = A/R^2$, and $\bar{\delta}(\bar{\mathbf{x}}) = R^3\delta(\mathbf{x})$.

APPENDIX C: WRINKLE PATTERNS

Mechanical instabilities in soft materials, specifically wrinkling, have led to the formation of unique surface patterns. Reference [34] discusses ten representative patterns of wrinkles, as shown in Fig. 9.

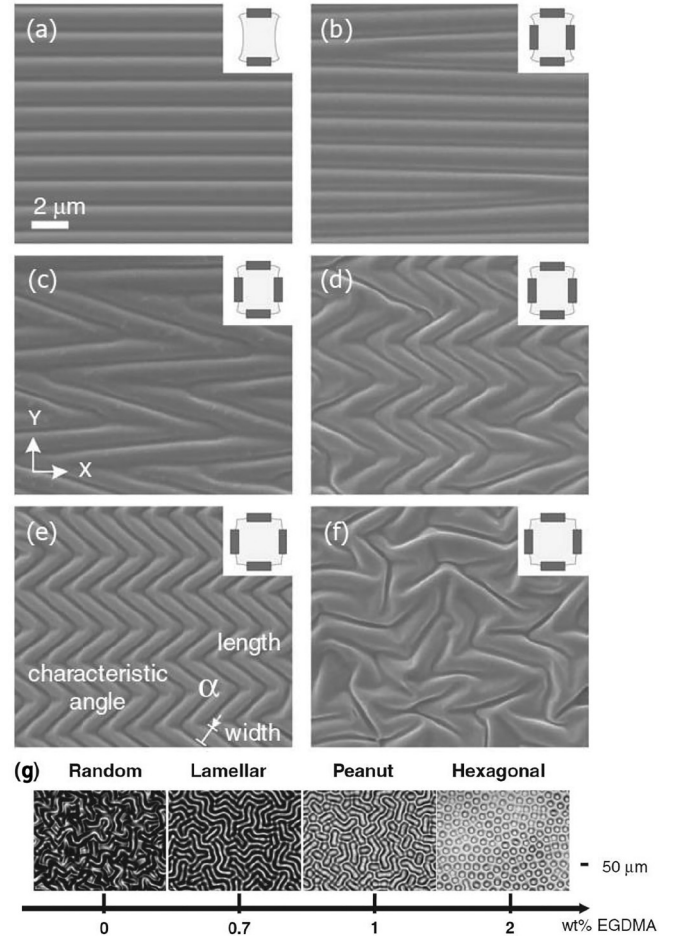


FIG. 9. Schematics of representative patterns of wrinkles: (a) ripples (a periodic array of straight wrinkles), (b) ripples with bifurcation, (c) truncated ripples with bifurcation (zigzag), (d) a more symmetrical zigzag herringbone structure, (e) herringbones (a periodic array of zigzag wrinkles), (f) a highly disordered zigzag herringbone pattern, and (g) from left to right, random wormlike structures, lamellar, peanut shape, and highly ordered hexagonal patterns, respectively. They are taken from Figs. 3 and 7(c) of Ref. [34].

- [1] S. EL Andaloussi, I. Mäger, X. O. Breakefield, and M. J. A. Wood, Extracellular vesicles: biology and emerging therapeutic opportunities, *Nat. Rev. Drug Discov.* **12**, 347 (2013).
- [2] H. Noguchi, Swinging and synchronized rotations of red blood cells in simple shear flow, *Phys. Rev. E* **80**, 021902 (2009).
- [3] H. Noguchi, Dynamic modes of red blood cells in oscillatory shear flow, *Phys. Rev. E* **81**, 061920 (2010).
- [4] U. Seifert, Fluid membranes in hydrodynamic flow fields: Formalism and an application to fluctuating quasispherical vesicles in shear flow, *Eur. Phys. J. B* **8**, 405 (1999).
- [5] F. Rioual, T. Biben, and C. Misbah, Analytical analysis of a vesicle tumbling under a shear flow, *Phys. Rev. E* **69**, 061914 (2004).
- [6] C. Misbah, Vacillating Breathing and Tumbling of Vesicles under Shear Flow, *Phys. Rev. Lett.* **96**, 028104 (2006).
- [7] P. M. Vlahovska and R. S. Gracia, Dynamics of a viscous vesicle in linear flows, *Phys. Rev. E* **75**, 016313 (2007).
- [8] D. Abreu and U. Seifert, Noisy Nonlinear Dynamics of Vesicles in Flow, *Phys. Rev. Lett.* **110**, 238103 (2013).
- [9] M. Guedda, Membrane compression in tumbling and vacillating-breathing regimes for quasispherical vesicles, *Phys. Rev. E* **89**, 012703 (2014).
- [10] K. Liu and S. Li, Nonlinear simulations of vesicle wrinkling, *Math. Meth. Appl. Sci.* **37**, 1093 (2014).
- [11] K. Liu, C. Hamilton, J. Allard, J. Lowengrub, and S. Li, Wrinkling dynamics of fluctuating vesicles in time-dependent viscous flow, *Soft Matter* **12**, 5663 (2016).
- [12] M. Kraus, W. Wintz, U. Seifert, and R. Lipowsky, Fluid Vesicles in Shear Flow, *Phys. Rev. Lett.* **77**, 3685 (1996).
- [13] J. Beaucourt, F. Rioual, T. Séon, T. Biben, and C. Misbah, Steady to unsteady dynamics of a vesicle in a flow, *Phys. Rev. E* **69**, 011906 (2004).
- [14] H. Noguchi and G. Gompper, Fluid Vesicles with Viscous Membranes in Shear Flow, *Phys. Rev. Lett.* **93**, 258102 (2004).
- [15] V. Narsimhan, A. P. Spann, and E. S. Shaqfeh, Pearling, wrinkling, and buckling of vesicles in elongational flows, *J. Fluid Mech.* **777**, 1 (2015).
- [16] A. Yazdani and P. Bagchi, Three-dimensional numerical simulation of vesicle dynamics using a front-tracking method, *Phys. Rev. E* **85**, 056308 (2012).
- [17] K. Liu, B. Chu, J. Newby, E. L. Read, J. Lowengrub, and J. Allard, Hydrodynamics of transient cell-cell contact: The role of membrane permeability and active protrusion length, *PLoS Comput. Biol.* **15**, e1006352 (2019).
- [18] K. H. de Haas, C. Blom, D. van den Ende, M. H. G. Duits, and J. Mellema, Deformation of giant lipid bilayer vesicles in shear flow, *Phys. Rev. E* **56**, 7132 (1997).
- [19] M. Abkarian, C. Lartigue, and A. Viallat, Tank Treading and Unbinding of Deformable Vesicles in Shear Flow: Determination of the Lift Force, *Phys. Rev. Lett.* **88**, 068103 (2002).
- [20] V. Kantsler and V. Steinberg, Orientation and Dynamics of a Vesicle in Tank-Treading Motion in Shear Flow, *Phys. Rev. Lett.* **95**, 258101 (2005).
- [21] V. Kantsler and V. Steinberg, Transition to Tumbling and Two Regimes of Tumbling Motion of a Vesicle in Shear Flow, *Phys. Rev. Lett.* **96**, 036001 (2006).
- [22] M. Mader, V. Vitkova, M. Abkarian, A. Viallat, and T. Podgorski, Dynamics of viscous vesicles in shear flow, *Eur. Phys. J. E* **19**, 389 (2006).
- [23] J. Deschamps, V. Kantsler, E. Segre, and V. Steinberg, Dynamics of a vesicle in general flow, *Proc. Natl. Acad. Sci. USA* **106**, 11444 (2009).
- [24] D. Kumar, C. M. Richter, and C. M. Schroeder, Double-mode relaxation of highly deformed anisotropic vesicles, *Phys. Rev. E* **102**, 010605(R) (2020).
- [25] M. Levant and V. Steinberg, Complex Dynamics of Compound Vesicles in Linear Flow, *Phys. Rev. Lett.* **112**, 138106 (2014).
- [26] D. Abreu, M. Levant, V. Steinberg, and U. Seifert, Fluid vesicles in flow, *Adv. Colloid Interface Sci.* **208**, 129 (2014).
- [27] O. Oshri, Delamination of open cylindrical shells from soft and adhesive winkler's foundation, *Phys. Rev. E* **102**, 033001 (2020).
- [28] V. Kantsler, E. Segre, and V. Steinberg, Vesicle Dynamics in Time-Dependent Elongation Flow: Wrinkling Instability, *Phys. Rev. Lett.* **99**, 178102 (2007).
- [29] K. S. Turitsyn and S. S. Vergeles, Wrinkling of Vesicles during Transient Dynamics in Elongational Flow, *Phys. Rev. Lett.* **100**, 028103 (2008).
- [30] R. L. Knorr, M. Staykova, R. S. Gracia, and R. Dimova, Wrinkling and electroporation of giant vesicles in the gel phase, *Soft Matter* **6**, 1990 (2010).
- [31] M. Levant and V. Steinberg, Amplification of Thermal Noise by Vesicle Dynamics, *Phys. Rev. Lett.* **109**, 268103 (2012).
- [32] K. Liu, J. Lowengrub, and J. Allard, Efficient simulation of thermally fluctuating biopolymers immersed in fluids on 1-micron, 1-second scales, *J. Comput. Phys.* **386**, 248 (2019).
- [33] C.-H. Wu, T. G. Fai, P. J. Atzberger, and C. S. Peskin, Simulation of osmotic swelling by the stochastic immersed boundary method, *SIAM J. Sci. Comput.* **37**, B660 (2015).
- [34] S. Yang, K. Khare, and P.-C. Lin, Harnessing surface wrinkle patterns in soft matter, *Adv. Funct. Mater.* **20**, 2550 (2010).
- [35] Z. Huang, W. Hong, and Z. Suo, Nonlinear analyses of wrinkles in a film bonded to a compliant substrate, *J. Mech. Phys. Solids* **53**, 2101 (2005).
- [36] J. S. Sohn, Y.-H. Tseng, S. Li, A. Voigt, and J. S. Lowengrub, Dynamics of multicomponent vesicles in a viscous fluid, *J. Comput. Phys.* **229**, 119 (2010).
- [37] K. Liu, G. R. Marple, J. Allard, S. Li, S. Veerapaneni, and J. Lowengrub, Dynamics of a multicomponent vesicle in shear flow, *Soft Matter* **13**, 3521 (2017).
- [38] C. S. Peskin, The immersed boundary method, *Acta Numer.* **11**, 479 (2002).
- [39] P. J. Atzberger, P. R. Kramer, and C. S. Peskin, A stochastic immersed boundary method for fluid-structure dynamics at microscopic length scales, *J. Comput. Phys.* **224**, 1255 (2007).
- [40] P.-O. Persson and G. Strang, A simple mesh generator in MATLAB, *SIAM Rev.* **46**, 329 (2004).
- [41] M. P. Allen and D. J. Tildesley, *Computer Simulation of Liquids* (Oxford University Press, New York, 2017), 2nd ed.
- [42] J. Cheng, M. Grossman, and T. McKercher, *Professional CUDA C Programming* (John Wiley & Sons, New York, 2014).

- [43] D. Kumar, C. M. Richter, and C. M. Schroeder, Conformational dynamics and phase behavior of lipid vesicles in a precisely controlled extensional flow, [Soft Matter](#) **16**, 337 (2020).
- [44] E. Evans and W. Rawicz, Entropy-Driven Tension and Bending Elasticity in Condensed-Fluid Membranes, [Phys. Rev. Lett.](#) **64**, 2094 (1990).
- [45] R. Finken, A. Lamura, U. Seifert, and G. Gompper, Two-dimensional fluctuating vesicles in linear shear flow, [Eur. Phys. J. E](#) **25**, 309 (2008).